Accepted Manuscript

Study of thermal behavior and solidification characteristics during laser welding of dissimilar metals

Zhiyong Li, Gang Yu, Xiuli He, Shaoxia Li, Haiming Li, Qingyu Li

PII: S2211-3797(18)32670-6
DOI: https://doi.org/10.1016/j.rinp.2018.12.017
Reference: RINP 1887

To appear in: *Results in Physics*

Received Date: 24 October 2018
Revised Date: 26 November 2018
Accepted Date: 3 December 2018

Please cite this article as: Li, Z., Yu, G., He, X., Li, S., Li, H., Li, Q., Study of thermal behavior and solidification characteristics during laser welding of dissimilar metals, *Results in Physics* (2018), doi: https://doi.org/10.1016/j.rinp.2018.12.017

This is a PDF file of an unedited manuscript that has been accepted for publication. As a service to our customers we are providing this early version of the manuscript. The manuscript will undergo copyediting, typesetting, and review of the resulting proof before it is published in its final form. Please note that during the production process errors may be discovered which could affect the content, and all legal disclaimers that apply to the journal pertain.

ACCEPTED MANUSCRIPT

Study of thermal behavior and solidification characteristics during laser welding of dissimilar metals.

Zhiyong Li[1, 2], Gang Yu[1, 2*], Xiuli He[1, 2*], Shaoxia Li[1],Haiming Li[2], Qingyu Li[1, 2]

1. Key Laboratory of Mechanics in Advanced Manufacturing, Institute of Mechanics, Chinese Academy of Sciences, Beijing 100190, China
2. School of Engineering Science, University of Chinese Academy of Sciences, Beijing 100049, China

Email: gyu@imech.ac.cn, xlhe@imech.ac.cn

Abstract

A transient three-dimension model was developed to study the thermal behavior and solidification characteristics during laser linear welding of 304ss and Ni considering the free surface deformation of the melt pool. The evolution of temperature and velocity field, the weld pool configuration and the solidification microstructure were investigated numerically and experimentally. A moving mesh method based on the Arbitrary Lagrangian Eulerian (ALE) was adopted to capture the free surface. Dimensional analysis was carried out to study the different heat transfer mechanisms. The solidification parameters, including the cooling rate (GR) and the morphological parameters (G/R), can be calculated through the transient thermal analysis to predict the solidification structure. The molten pool configuration on both sides changed from circular to elliptical as a result of the change of the dominant heat transfer mechanism. Sharp changes of the curvatures of the weld pool boundary were also observed and explained by the Prandtl number. Because the G/R was bigger at the bottom and the GR was larger at the top surface of the molten pool, the microstructure morphology changed from equiaxed dendrites to cellular dendrites to planar, and grain size increased from the top area to the bottom in 304ss side. The similar phenomenon was also observed in Ni side.

Key words: Laser welding；Dissimilar metals；ALE；Thermal behavior；Solidification characteristics

1.Introduction

Welding of dissimilar alloys in products provides great flexibility for the designers and engineers，which may satisfy both the mechanical and economic requirements of fabricated products [1-3]. For example，the joining of relative expensive anti-corrosion nickel and less expensive 304 stainless steel is widely used in the petrochemicals, the high pressure containers and the aerospace. However, defects such as the asymmetric weld pattern，the formation of intermetallic brittle phase and the improperly mixed weld metals are still serious challenges in dissimilar welding. These problems are generally caused by the differences in mechanical, thermal-physical and metallurgical properties of the alloys, such as the thermal conductivity, the specific heat of both solid and liquid, the temperature coefficient of surface tension and the coefficient of thermal expansion [4-8]. Fundamental study of thermal behavior and solidification characteristics in this investigation could be used to predict the microstructure and possible defects, and hence, improve the weld quality.

ACCEPTED MANUSCRIPT

Thermal behavior in the weld pool had been the subject for many researches in the past decades. Progress had been made on the heat transfer and fluid flow in different fusion welding processes including gas tungsten arc (GTA) welding [9–15], gas metal arc (GMA) welding [16–18] and laser welding [19-20] for similar alloys. However, there were not so many researches focused on thermal behavior for welding of dissimilar alloys[21-22], especially on laser dissimilar welding[23]. A.Bahrami et al [21] studied the fluid flow in the weld pool for the GTA spot welding of 1018 steel and nickel 200. It was demonstrated that the effect of temperature gradient is more significant in determining the Marangoni shear stress. Wei and Chung [22] studied the effect of Marangoni convection in the molten pool during the high energy beam welding and introduced a dimensionless number that determines the importance of surface tension effects in dissimilar welding. They found that convection was driven by Marangoni forces with different directions and magnitudes on a flat free surface. Hu et al [23] established a mathematical model to simulate the driving forces of molten metal flow in the laser spot welding of stainless steel and nickel. It was observed that the temperature coefficient of surface tension of stainless steel has greater impact on the molten pool configuration than that of nickel. The great importance of Marangoni convection in the welding process was illustrated by all the studies above.

Although some achievements on thermal behavior had been made for laser dissimilar welding, the three-dimensional deformation of the melt pool surface was ignored in numerical models mentioned above, which may change the boundary conditions and then affects the heat transfer and fluid flow in the molten pool. Besides, the solidification parameters, which had great effect on final microstructure and properties, had been ignored for simulation in laser dissimilar welding. Wang et al [24] numerically and experimentally investigated the relationship between thermal behavior and solidification microstructure in GTAW of AA1060, and the influence of variable polarity on microstructure was studied through the analysis of the solidification parameters. In addition, the welding parameters, especially the welding speed, may greatly affect the thermal behavior and solidification characteristics [25,26]. However, previous research was focused on the laser spot welding of dissimilar metals [23], and the thermal behavior and solidification characteristics have not been studied sufficiently during the laser linear welding of dissimilar alloys. Although the study of laser spot welding provided a fundamental insight into the heat transfer mechanism, the linear welding is more widely used in industrial fabrication and the

ACCEPTED MANUSCRIPT

numerical models for these two welding processes were quite different.

In this study, a transient three-dimensional model, including the heat transfer, the fluid flow, the solidification and the free surface of the melt pool was developed to study the laser dissimilar welding process. The free surface was captured by a moving mesh method based on the Arbitrary Lagrangian Eulerian (ALE) [27,28], which had been introduced by Gan et al [29] in a 3D model to capture the liquid/gas interface of the molten pool during the direct laser deposition. Considering the time dependent boundary caused by the three dimensional deformation, the transient temperature distribution and the velocity field were obtained more accurately. The influence of Marangoni convection was studied from 2D and 3D views by introducing the streamlines to characterize the convection. Dimensionless analysis method was also adopted to understand the relative importance of various boundary layers and the dominant heat transfer mechanisms at different times. The solidification parameters GR and G/R were calculated through thermal analysis to predict the solidified microstructure. The effect of welding speed on the solidification microstructure was also studied through the solidification parameters mentioned above. The calculated weld pool configuration and the predicted microstructure were then compared with the experimentally observed results to verify the model, respectively.

2. Experiment procedure

The industrial pure nickel N6 and 304 stainless steel were used in laser heat conduction welding experiments. Experiments were conducted on a Nd: YAG continuous laser processing system with a five-axis CNC working system. In this study, the laser spot radius on the top surface of the welding specimens was 0.57mm, and the laser power used in experiment was 800W. Pure argon with the flow rate of 15L / min was used as the shielding gas. The welding speed adopted in the experiment varies from 10mm/s to 30mm/s, with an interval of 5mm/s. The dimension of the samples used for welding was 80mm × 40mm × 2mm and the chemical composition was shown in Table.1.

Table.1 Chemical composition of 304ss and Ni (atomic fraction (%))

Material	C	P	S	Cr	Ti	Ni	Fe
N6	0.081	-	0.015	-	0.056	99.7~99.8	0.062
304ss	≤0.08	≤0.045	≤0.03	18~20	-	8~10.5	Bal

ACCEPTED MANUSCRIPT

Before the experiment, the surfaces of the welding samples were cleaned by acetone to avoid the oil and other impurities. Metallographic samples were prepared by sectioning the welded pieces across the welding seam using electric discharge cutting machine. The samples were ground and polished using standard mechanical polishing procedures and then etched in a HCL:HNO_3 solution with a volume ratio of 3:1. The treated specimens were then characterized by light microscope (OM) and scanning electron microscopy(SEM) .

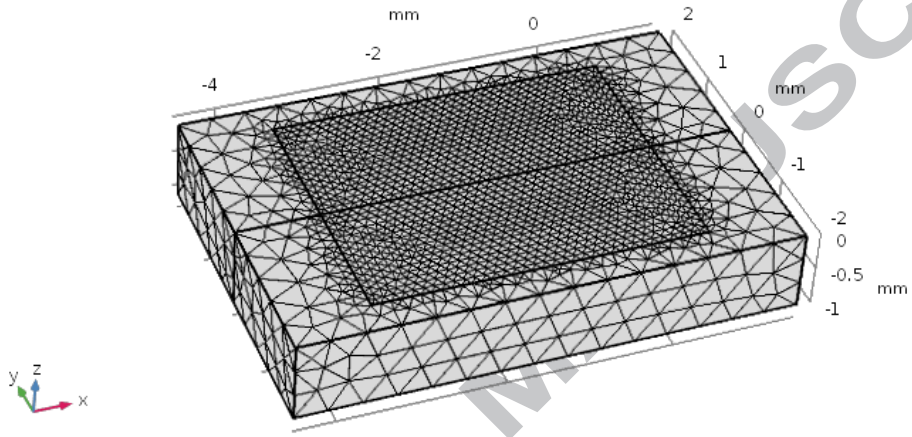

Fig.1 Model geometry and mesh grids for numerical simulation

3. Mathematical modeling

3.1 Major assumptions

A three-dimensional numerical model is developed to investigate the heat transfer and fluid flow in laser butt welding of dissimilar metals of 304ss and Ni couple. The mathematical model was formulated under following assumptions:

1. The flow of the liquid metal is assumed to be Newtonian, laminar and incompressible. The Boussinesq approximate is used to account for the density change due to the temperature variations.

2. The laser heat flux at the top surface of the workspace is assumed to be a Gaussian distribution.

3. The mushy zone, where the temperature is between the solidus and liquids, is assumed as a porous medium.

4. Thermal contact resistant between the two work pieces is not considered.

5. Relevant physical and thermal properties of the molten pool metal are assumed to be temperature related, and vary linearly with temperature.

ACCEPTED MANUSCRIPT

3.2 Governing equations

Based on above assumptions, the equations of conservation of mass, momentum-transport and thermal energy are simulated as Eq.(1), Eq. (2) and Eq.(5).

The equation of conservation of mass is:

$$\frac{\partial \rho}{\partial \mathrm{t}}+\frac{\partial(\rho u_i)}{\partial x_i}=0 \tag{1}$$

The momentum-transport equation is:

$$\frac{\partial\ (\rho \mathrm{u}_i)}{\partial t}+\frac{\partial(\rho u_i u_j)}{\partial x_{\mathrm{j}}}=\frac{\partial}{\partial x_j}(\mu\frac{\partial u_i}{\partial x_j})+\frac{\partial}{\partial x_i}(\mu\frac{\partial u_i}{\partial x_i})-\frac{\partial p}{\partial x_i}+\rho \mathrm{g}\beta_T(T-T_{ref})+F_d \tag{2}$$

where ρ and μ represent the density and viscosity of the fluid, respectively. The properties β_T and T_{ref} are the temperature volumetric expansion factor and the reference temperature, respectively. u_i is the velocity vector, and p is the pressure. F_d represents the frictional dissipation of momentum in the mushy zone according to the Carman-Kozeny equation for flow through porous media [33-34].

F_{d} is defined as follow:

$$F_{\mathrm{d}}=\frac{(1-f_l)^{\ 2}}{f_l^{\ 3}+\varepsilon_m}K_m u_i \tag{3}$$

In this simulation, f_l is the liquid fraction, K_m is a numerically large number and ε_{m} is a small number to avoid the division f_l by zero. The liquid fraction is given as:

$$\mathrm{f}_l=\begin{cases}0, & 0<T<T_s\\ \dfrac{T-T_s}{T_l-T_s}, & T_s<T<T_l\\ 1, & T>T_l\end{cases} \tag{4}$$

where T_{l} and T_S are the liquids and solidus temperatures, respectively. The thermal energy equation is:

$$\frac{\partial\ (\rho \mathrm{c}_p T)}{\partial t}+\frac{\partial(u_i \rho \mathrm{c}_p T)}{\partial x_i}=\frac{\partial}{\partial x_i}(K\frac{\partial T}{\partial x_i})-\frac{\partial(\rho\Delta H)}{\partial t}-\frac{\partial\ (\rho \mathrm{u}_i\Delta H)}{\partial x_i} \tag{5}$$

where c_{p} is the specific heat, and K is the thermal conductivity, H is the latent enthalpy content

ACCEPTED MANUSCRIPT

of the fusion, which is given as,

$$\Delta H = L\mathrm{f}_l \tag{6}$$

where L denotes the latent heat of fusion.

Material properties and processing parameters used for calculation are presented in Table.2 and Table.3, respectively.

Table.2 Material properties of 304ss and nickel [30,31]

Property	304ss	Ni
Liquidus temperature (K)	1727	1735
Solidus temperature (K)	1672	1730
Heat of fusion (kJ/kg)	272	290
Specific heat of solid ($J/kg\cdot K$)	711.28	515
Specific heat of liquid($J/kg\cdot K$)	836.8	595
Thermal conductivity of solid($W/m\cdot K$)	19.2	60.7
Effective thermal conductivity of liquid($W/m\cdot K$)	50	150
Density of solid metal (kg/m^3)	7450	8900
Density of liquid metal (kg/m^3)	6910	8880
Dynamic viscosity ($kg/m\cdot s$)	6.70×10^{-3}	3.68×10^{-3}
Surface tension (N/m)	1.872	1.778
Temperature coefficient of surface tension ($N/m\cdot K$)	-4.30×10^{-4}	-3.40×10^{-4}

Table. 3 Parameters applied in calculation [32]

Parameter	Value
Power distribution factor	2
Laser absorption efficiency	0.5
Ambient temperature	300 K
Convective heat transfer coefficient at top surface	$100(W/\mathrm{m}^2\cdot K)$
Emissivity	0.2
Stefan-Boltzmann constant	$5.67\times10^{-8}(W/\mathrm{m}^2\cdot K^4)$

3.3 Boundary conditions

The laser heat flux at liquid/gas interface is described as:

$$\mathrm{q}_{ener} = \frac{2\mathrm{Q}_\mathrm{e}}{\pi r_\mathrm{b}^2}\exp(-\frac{2r^2}{r_b^2}) - h_c(T-T_0) - \sigma_b\varepsilon(T^4-T_0^4) \tag{7}$$

where Q_e is the absorbed laser power which depends on nominal laser power and absorption efficiency of the material. The properties r and r_b are the distance from the grid node to the

ACCEPTED MANUSCRIPT

center of the laser beam and the effective radius of the laser beam, respectively. The third term in the right hand of Eq.7 is the heat convection loss and h_c is the heat transfer coefficient. The fourth term in the right hand of Eq.7 is the radiation loss, where σ_b is the Stefan-Boltzman constant, ε is the emissivity, and T_0 is the ambient temperature.

Boundary Conditions of the momentum equation at the liquid/gas interface is described as:

$$F_{L/G} = \sigma \mathbf{n}^* \kappa - \nabla_s T \frac{d\sigma}{dT} \tag{8}$$

The two terms on the right hand in the Eq. (8) represent the capillary force and the thermocapillary force, respectively. σ is the surface tension, n^* is the normal of surface, and κ is the curvature of surface.

To capture the free surface of the weld pool, a moving mesh method based on the ALE is used in this investigation. The mathematical principle of this method will be covered in the following discussion. The velocity of liquid/gas interface can be described as:

$$V_{L/G} = \mathbf{u}_{L/G} \cdot \mathbf{n}^* \tag{9}$$

where $\mathbf{u}_{L/G}$ is the velocity at the liquid/gas interface.

In this study, the model geometry and mesh grids for numerical simulation was shown in Figure 1. Quadratic polynomials were used for the discretization for the whole domain and SIMPLE solver was used to solve all the equations. Finer unstructured tetrahedral mesh with a maximum mesh size of 80 μm and coarser tetrahedral mesh with a maximum mesh size of 400 μm were applied in the fluid domain and solid domain, respectively. The mesh grids consist of 13884 nodes and 79191domian units, and a maximum time step of 0.1 ms was employed. This model was computed using a Dell T5500 computing station (12 × 2.5 GHz–24 GB), and each simulation took approximately 60h to complete.

4.Results and discussion

4.1 Heat transfer and fluid flow

Fig.2(a)-(d) show the computed temperature and fluid flow distribution at different times. In the figures, temperature field is indicated by the contour and two isotherms represent liquidus temperature of 304ss and nickel, respectively. At the initial stage of the welding process, the

ACCEPTED MANUSCRIPT

temperature raises quickly and the maximum temperature exceeds the melting points of the base metals. The solid-liquid phase change occurs and leads to the development of the melt pool.

During the welding of dissimilar metals, the heat transfer phenomena is mainly influenced by the thermal conduction and the convection caused by fluid flow. The relative importance of the two mechanisms can be measured by the dimensionless number of Peclet number:

$$Pe_T = \frac{heat_{convection}}{heat_{conduction}} = \frac{\rho u L_R \mu}{\mu \rho \alpha} = \frac{u L_R}{\alpha} \tag{10}$$

where u is the characteristic liquid velocity in the melt pool, L_R is the characteristic length taken as the melt pool radius, and α is the thermal diffusivity of material.

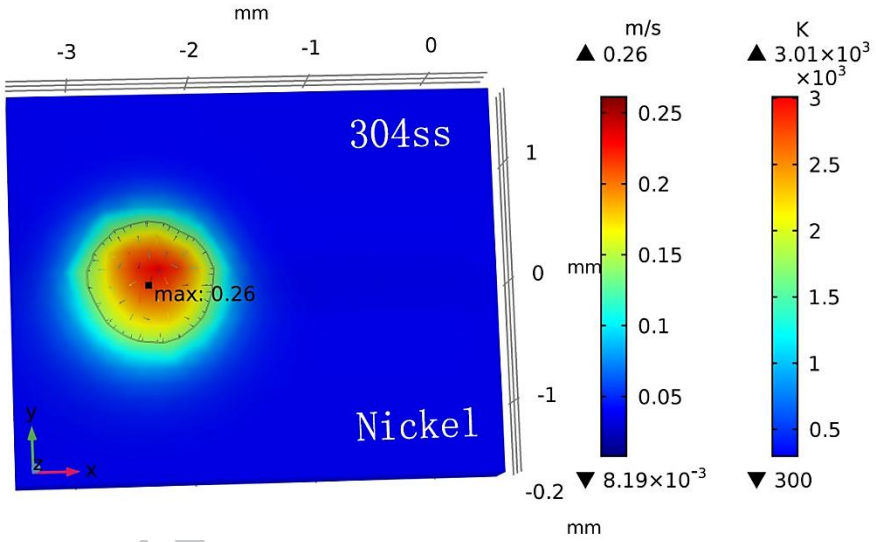

(a) 10ms

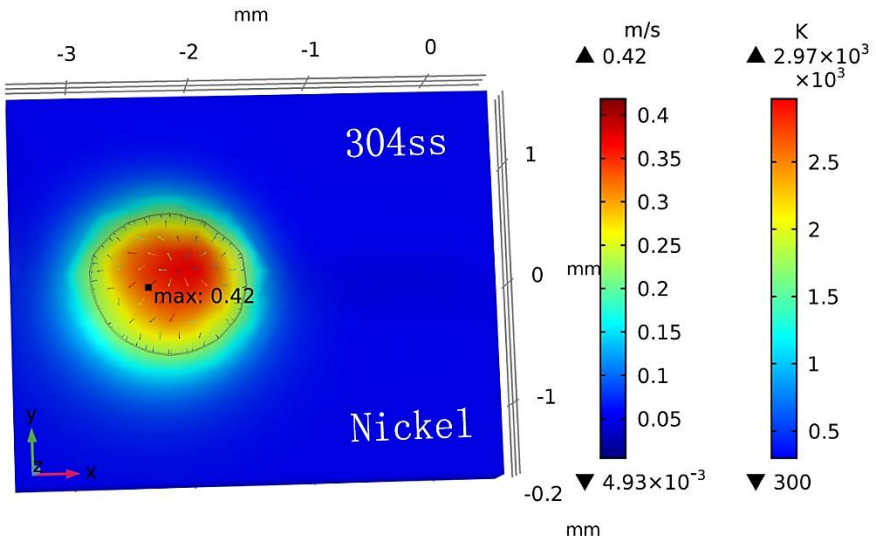

(b) 20ms

ACCEPTED MANUSCRIPT

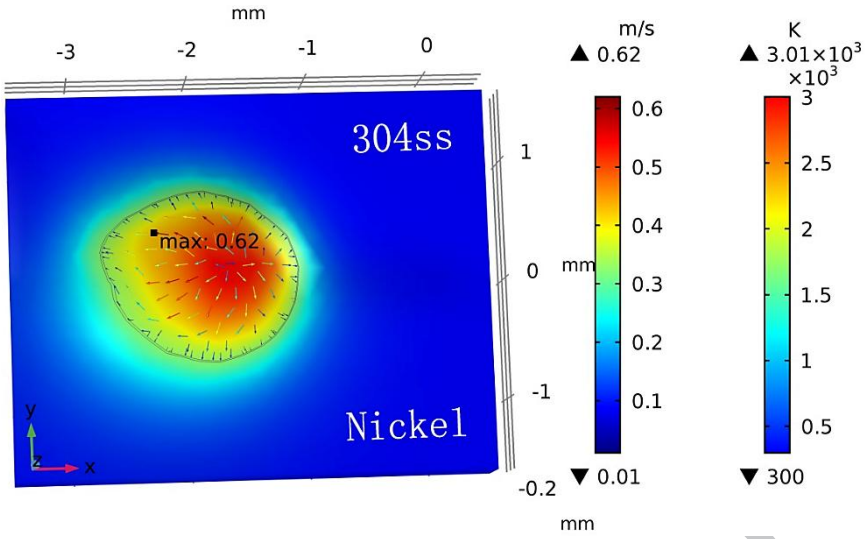

(c) 40ms

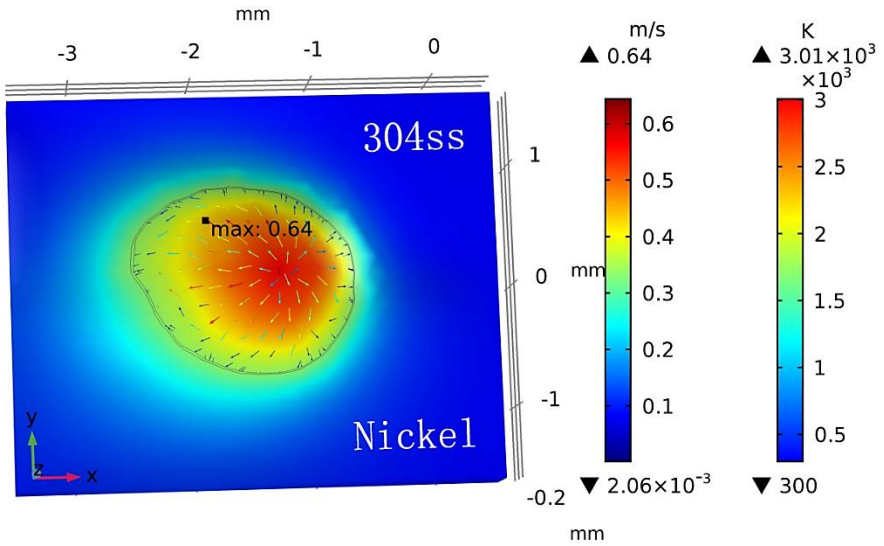

(d) 60ms

Fig.2 Computed temperature and fluid flow field with the welding speed of 20mm/s. (a) 10ms. (b)20ms. (c)40ms. (d)60ms

The velocity field at the top surface of the weld pool at various times during the laser welding process is also shown in Fig.2. The velocity distribution is characterized by arrows. As illustrated in Fig.2(a)-Fig.2(d), the velocity and the computed Peclet number are small at the initial stage, the weld pool on both sides are approximately circular for the dominant heat transfer mechanism is conduction. As the processing proceeds, a strong outward Marangoni convection is induced and the weld pool configuration reaches steady state due to the Marangoni convection. The melt pool flows fully and the maximum velocity of the molten pool reaches 0.42m/s at the time of 20ms, as shown in Fig.2(b). Under the condition, the Pe_T is calculate to be 46 for 304ss (13 for nickel),

ACCEPTED MANUSCRIPT

thus the dominant heat transfer mechanism changes from heat conduction to convection. As seen in Fig.2(c) and Fig.2(d), the maximum velocity is more than 0.6m/s, and the weld pool configuration keeps stable under the heat transfer mechanism of convection. When the molten pool reaches steady state, it is not symmetric and the fluid metal is driven from the center towards the fusion boundary for the negative coefficient of surface tension. As illustrated above, the molten pool configuration on both sides change from circular to elliptical, but because of the difference in thermal physical parameters, the shape of the molten pool on both sides is still quite different. The area of the melt pool in 304ss side is bigger due to lower thermal conductivity and melting temperature. After 60 ms, the melt pool reaches a steady condition. From this time on, the dimensions and morphology of the melt pool change little and its shape will remain almost constant as well.

In addition，it should be noted that the maximum velocity appears at 304ss side after the weld pool is stable as a result of much higher surface tension. The surface tension and temperature coefficient of surface tension are listed in Table.2. Though the surface tension decreases faster for 304ss due to the larger temperature coefficient of surface tension, the surface tension for 304ss is still higher than that for Ni in the range of the temperature of the weld pool. Therefore, higher velocity is induced by stronger driving force.

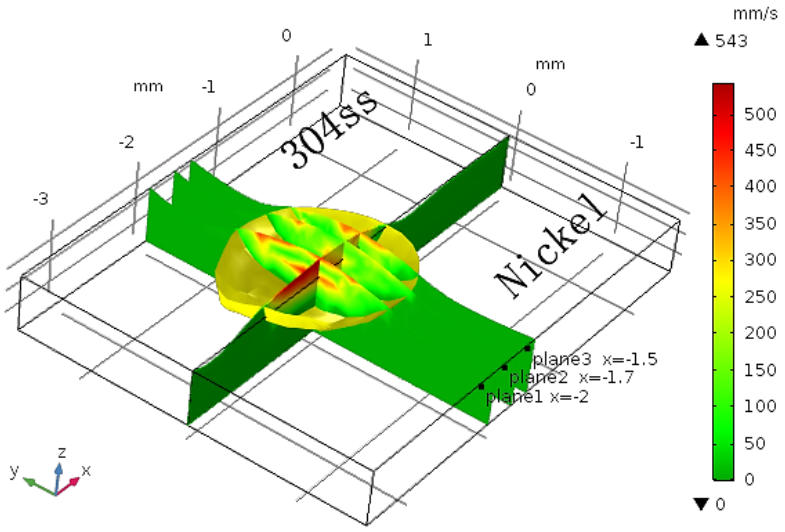

Fig.3 Weld pool profile and the velocity distribution on four representative planes.

ACCEPTED MANUSCRIPT

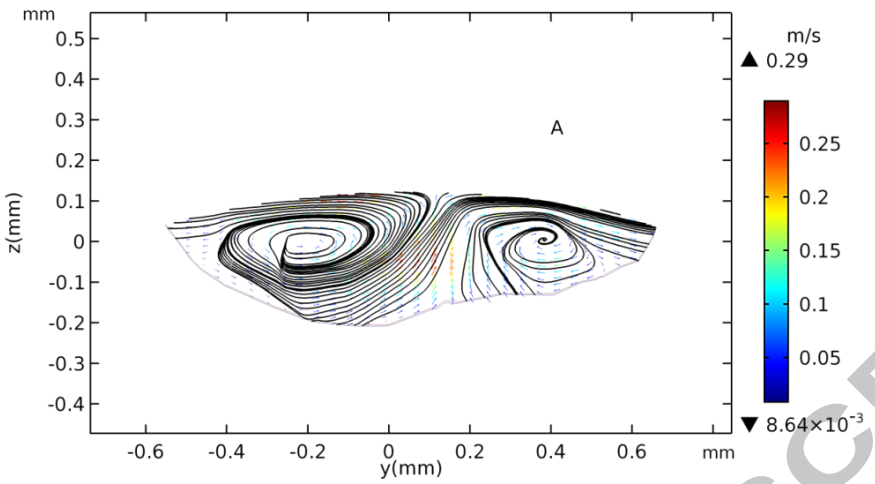

(a) plane1, x=-2mm

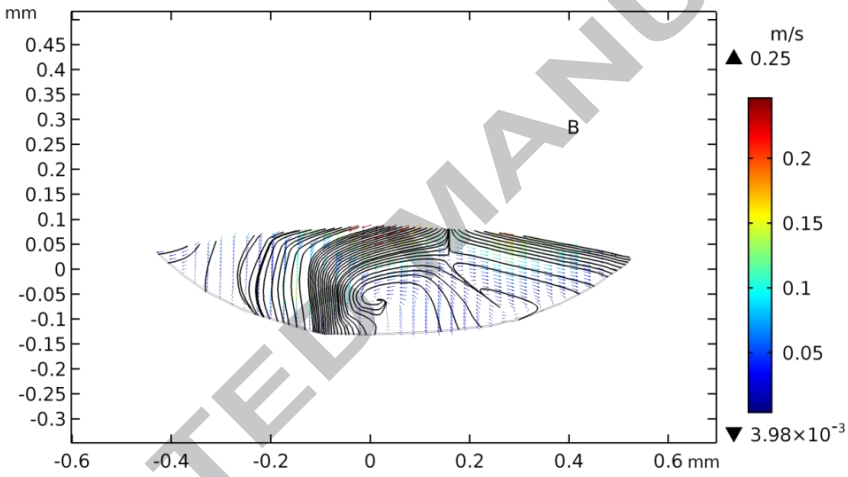

(b) plane2, x=-1.7mm

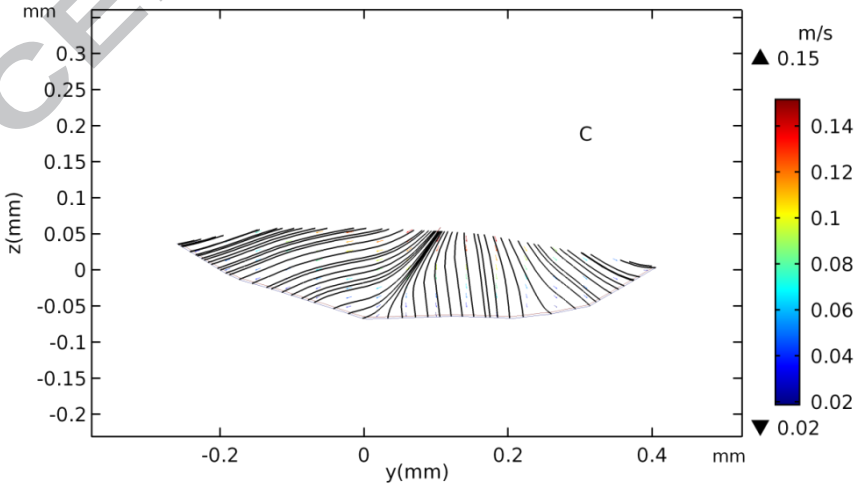

(c) plane3, x=-1.5mm

Fig.4 The velocity field and streamlines at three yz cross sections. (a) plane1. (b)plane2. (c)plane3.

ACCEPTED MANUSCRIPT

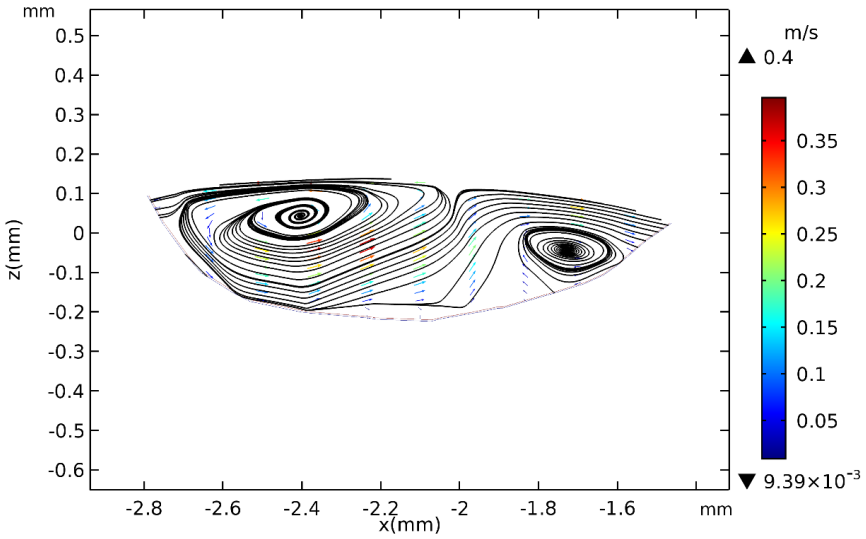

Fig.5 The velocity field and streamlines at xz-plane

The velocity fields at three different planes parallel to the yz-plane and the symmetry plane of xz-plane are investigated to provide more details about the fluid flow in the melt pool, as shown in Fig.3. The initial location of the laser beam is x=-2.5mm and the welding speed is 20mm/s in this simulation. Plane 1 is located at x=-2mm, plane2 is located at x=-1.7mm, plane3 is located at x=-1.5, and the center of the laser heat source is exactly at the location of x=-2mm at the time of 25ms. The velocity is shown via a color map. As can be seen from Fig 3, the velocity distribution is swirling due to intense Marangoni convection, and the vital influence of the convection on fluid flow is verified here.

The velocity fields in three planes parallel to the yz-plane, shown in Fig.3, are presented in Fig.4, and streamlines are also introduced to analyze the flow field evolution. For plane 1 (x=-2mm), shown in Fig.4(a), there are obviously two separate vortical motions on both sides. For plane 2, shown in Fig.4(b), the vortices become weaker and the fluid partly flows toward the Ni side. The fluid motion at plane 3, shown in Fig.4(c), is generally weaker on both sides. The weld pool is much wider and deeper in Fig.4(a) than that in Fig.4(b) and Fig.4(c) because the plane 1 is exactly under the center of the laser beam at the time of 25ms. For symmetric plane, the interface of 304ss and Ni, shows in Fig.5, there are also two separate vortical motions and the fluid partly flows towards the welding direction. Fig.4 and Fig.5 provide visual 2D views and further understanding of complicated 3D heat transfer and fluid flow in the weld pool.

Under the assumption of incompressible fluids, the magnitude of the velocity can be characterized by the density of the streamlines. The streamline is the curve tangent to the velocity

ACCEPTED MANUSCRIPT

vector at each point in the flow field, and it gives the velocity direction of different fluid particles at this moment. The velocity is fast where streamlines are dense; on the contrary, the velocity is slow. As illustrated in Fig.4(a) and Fig.4(d), streamlines near the circular vortex are denser and higher velocity is introduced here due to the intense Marangoni convection. Though no obvious vortical motions are observed in Fig.4(b) and Fig.4(c), it can also be shown that there is higher velocity where streamlines are dense. The streamlines reveal the influence of the Marangoni convection on fluid flow in melt pool from another view.

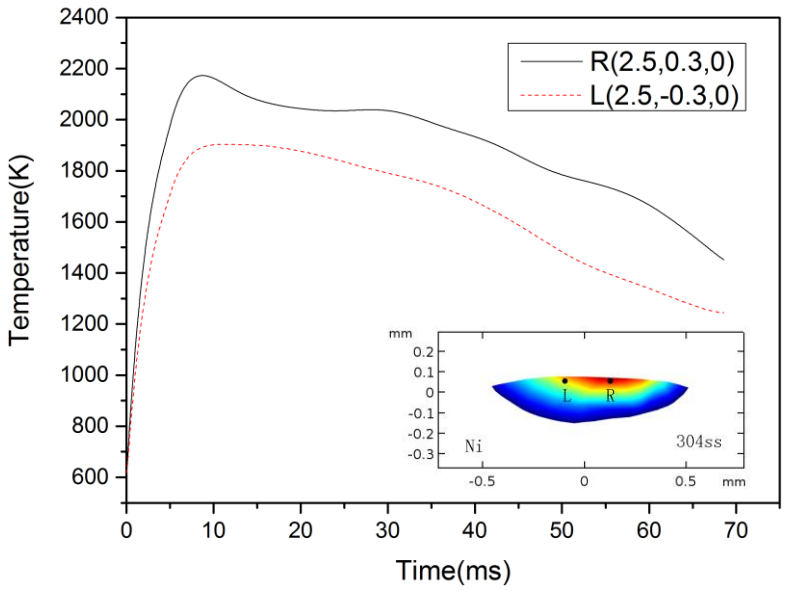

Fig.6 Thermal history of two representative points in the molten pool

According to the general welding mechanic theories， the welding residual stress and deformation are both greatly influenced by the welding temperature history and temperature gradient during the fusion and solidification process. Fig.6 shows the evolution of two representative points, whose geometry coordinates in the model are (-2.5,0.3,0) and (-2.5, -0.3,0) in millimeter, respectively. The difference of temperature evolution between the two points is significant as seen from Fig.6. In the heating stage, the maximum temperature in 304ss side is higher than that in the nickel side; In the cooling stage, the cooling rate in 304ss side is much higher within a few milliseconds after the laser sweeps. This phenomenon can be explained by the lower thermal conductivity of 304ss and the rapid solidification of the molten pool after the heat source swept. The heat transfer mechanism is heat conduction in the cooling stage and the higher

ACCEPTED MANUSCRIPT

thermal conductivity of nickel makes the temperature gradient decrease, thus the cooling rate is smaller at Ni side.

Besides, it can also be seen that the difference of temperature evolution between the two representative points during the heating phase is significantly smaller compared with the cooling phase. This can be attributed to the fluid flow in the weld pool. During the heating stage, the heat transfer is dominated by convection and the influence of thermal physical parameters on the heat transfer is reduced, so that the temperature difference on both sides is smaller. For the temperature history of one point, the temperature change rate in the heating phase is much greater, which can also be explained by the heat transfer mechanism of convection caused by intense Marangoni convection in the heating phase.

4.2 Weld pool configuration

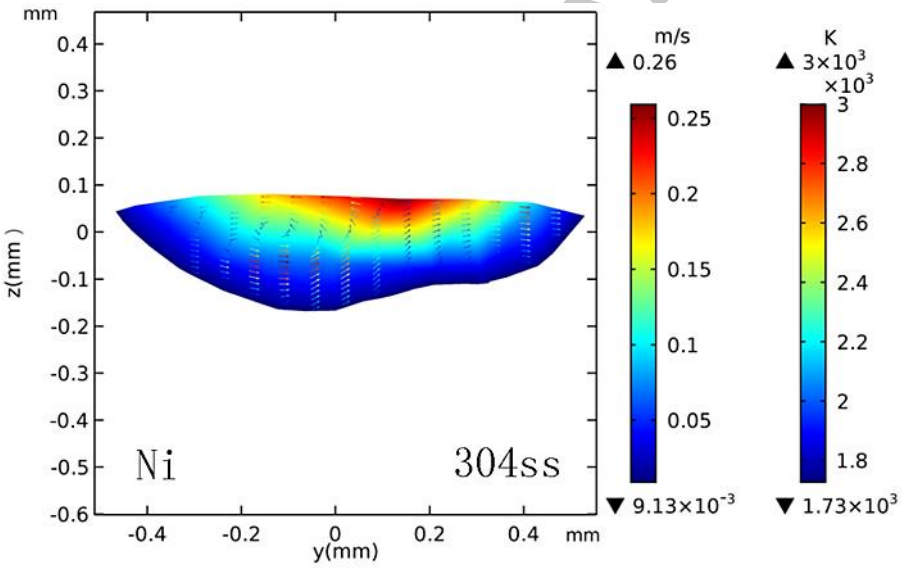

(a) Calculated weld pool profile

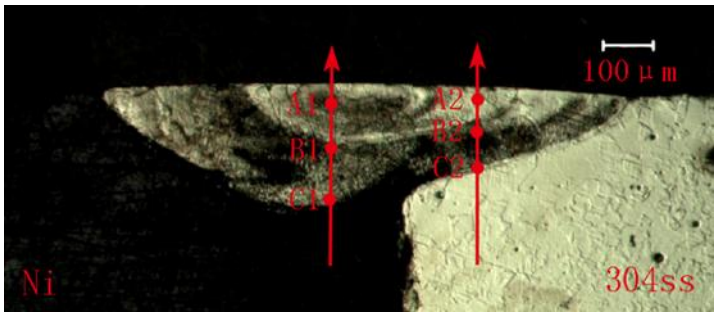

(b) Experimental weld pool profile

Fig.7 Comparison of the experimental and numerical weld pool profile. (a) Calculated weld pool

ACCEPTED MANUSCRIPT

profile. (b) Experimental weld pool profile

During laser linear welding process, surface tension directly acts on the upper surface, buoyancy acts on the entire molten pool. At the same time, a great change in material properties is induced by the solid-liquid phase transition. Therefore, a three-dimensional deformation occurs on the molten pool surface under the combined effect of the factors mentioned above. It will change the heat transfer conditions in the molten pool, and then affect the temperature distribution and velocity field in the melt pool. Therefore, it is necessary to study the free surface deformation during laser linear welding. However, consideration of the free surface deformation will greatly increase the difficulty of the simulation, hence, the surface is assumed to be flat in most studies of heat transfer and fluid flow in the molten pool [21-24].

To capture the free surface deformation caused by multi-physics factors, a suitable numerical simulation method should be sincerely considered. The Lagrangian formulation, where the mesh moves with the material, can solve problems in solid mechanics accurately. The Eulerian formulation, where the mesh is fixed in space, is commonly used to solve problems in fluid mechanics [28]. However, the Lagrangian method cannot handle large deformation of the fluid and the Euler method sacrifices accuracy when used for solid. Consequently, for problems involving fluid and structure, such as the gas/liquid interface of the weld pool, neither the Lagrangian nor the Eulerian formulation can be used for the entire domain. Therefore, the moving-mesh method based on the ALE is adopted in this investigation, which allows the mesh to move in arbitrary manner and permits the mesh to transit from being Eulerian for modeling the fluid flow to a nearly Lagrangian that follows the deformation of the structure.

The ALE method is numerically economical and resolves the material boundaries and free surface accurately. The governing equations based on the ALE formulation are derived as follow [28]:

$$\frac{\partial J\rho \mathbf{f}}{\partial t} = J\rho \dot{f} - J\frac{\partial \rho f \partial w_i}{\partial x_i} \tag{11}$$

$$\frac{\partial \rho J}{\partial t} = -J\frac{\partial \rho w_i}{\partial x_i} \tag{12}$$

$$\frac{\partial \rho J u_i}{\partial t} = J(\sigma_{ij,j} + \rho b_i) - J\frac{\partial \rho u_i w_j}{\partial x_j} \tag{13}$$

ACCEPTED MANUSCRIPT

$$\frac{\partial \rho Je}{\partial t} = J(\sigma_{ij} u_{i,j} + \rho b_i u_i) - J\frac{\partial \rho e w_j}{\partial x_j}$$

(1 4)

where u is the velocity of the material and v is the velocity of the reference coordinate. Their difference, u − v, is denoted w. The Jacobian, J, is the relative differential volume between the reference and the spatial coordinates. σ_{ij} is the stress tensor, and b_i is the physical component. Eq. (11) is the ALE equation for general variable f written in its general form. The first term on the right-hand side of eq. (11) is the source term for f, and the second term, the transport of f. Eq. (12) to eq. (14) are the conservation form of the ALE equations. When w is zero, J is 1 and the Lagrangian equations are recovered from equation (12). If the reference coordinates are the current spatial coordinates, w is v, J is again 1, and the Eulerian equations are recovered.

Numerical model is validated by comparing the simulated and experimentally observed cross section of the weld pool. Deformation of free surface was considered and a moving mesh method based on ALE method was used in numerical model to capture the free surface. The calculated free surface shown in Fig.7(a) is reasonably consistent with the experimentally observed result shown in Fig.7(b).

Sharp changes of curvatures of the weld pool boundary are also observed from Fig.7 since the intense competition between the heat transfer mechanism of convection and conduction. The phenomenon can be explained by the relative thickness of momentum and thermal boundary layers, which can be represented by the dimensionless number of Prandtl number：

$$P_r = \frac{\mu C_p}{K} \tag{15}$$

According to the material properties listed in Table.2, the computed Pr is 0.25 for 304ss and 0.0028 for Ni. Therefore, the role of heat transfer boundary layer is significantly important in Ni side and intense competition of heat thermal boundary layers and momentum boundary layers would occur in 304ss side. Thus, the fusion boundary in Ni side is approximately circular and two inflexions of the fusion boundary in 304ss side could be observed as a result of the competition. Besides, the Marangoni convection mainly acts at the upper part of the melt pool, and the bottom boundary is concave, dominated by heat conduction in Ni side since the Pr is far lower than 1.

ACCEPTED MANUSCRIPT

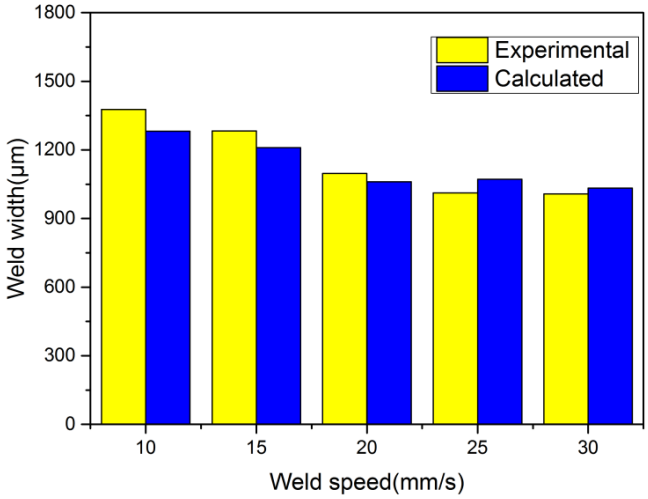

(a) Weld width

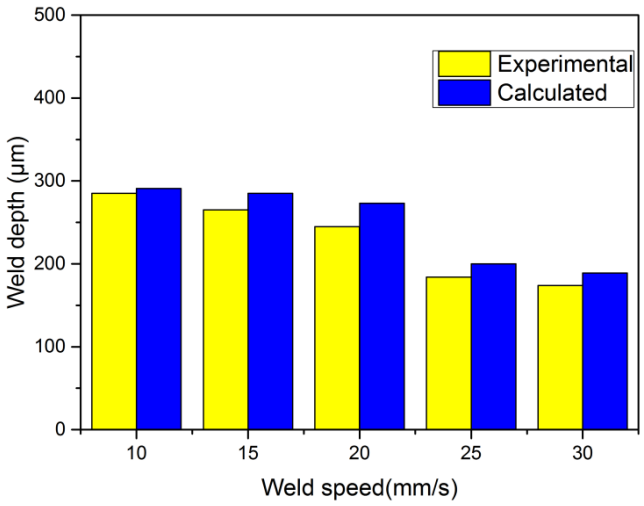

(b) Weld depth

Fig.8 Weld dimensions under different welding speed. (a) weld width. (b) weld depth

Fig.8 shows the weld dimensions under different welding speed. With an increase of weld speed from 10 to 30 mm/s, both the weld width and weld penetration decrease. As shown in Fig.8, both the experimental and simulated weld width and depth are in reasonable agreement with relatively small errors. The calculated weld width may be larger or smaller compared with the experimental results, and the calculated weld depth is a little larger than the experimental depth. It was mentioned before that the simulation was investigated under the assumption of Newtonian laminar flow, and the relative importance of laminar flow and turbulent flow can be evaluated by the Reynolds number. Reynolds number is described as the ratio of inertial force and viscous force,

ACCEPTED MANUSCRIPT

and it is calculated as:

$$\mathrm{Re} = \frac{\rho u L_R}{\mu} \tag{16}$$

where ρ is the density of liquid metal. The calculated Reynolds number in the molten pool is on the order of 1000, thus the turbulent flow may have influence on the results. Therefore, one of the reasons that the calculated weld penetration is larger as illustrated in Fig.8(b) may be the ignorance of turbulent flow. Besides, according to the study of Hong et al [26] for a GTA weld in a 304ss, a fluid flow based on laminar flow can over-predict the pool depth. Both the effective viscosity and the effective thermal conductivity increase when turbulence is considered. Consequently, the convention motion slows down and the influence of heat conduction increases, thus the melt pool penetration decreases compared with the calculated result under the assumption of laminar flow.

4.3 Solidification characteristics

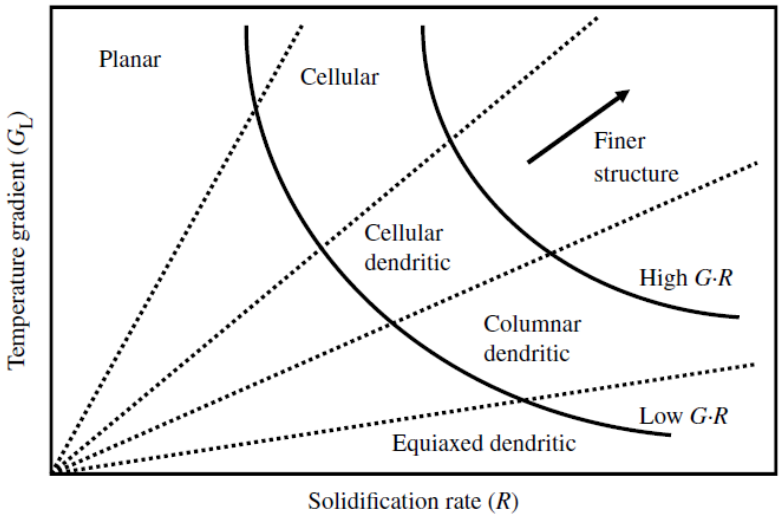

Fig.9 The effects of the G and R on the morphology and scale of the solidified microstructure [25].

The solidified microstructure is greatly affected by the solidification parameters of temperature gradient G、solidification rate R and their combinations GR and G/R. The units of GR and G/R are K/s and $K \cdot s/mm^2$, respectively. As shown in Fig.9, the solid-liquid interface stability factor G/R, is related to the solidification morphology, while the cooling rate GR influences the scale of the solidification microstructure. As G/R increases, the interface morphology changes from equiaxed-dendritic to cellular-dendritic to cellular grains. On the other hand, dendrites of finer size

ACCEPTED MANUSCRIPT

occur under higher cooling rate.

Fig.10(a) shows the microstructure of representative points of A1, B1 and C1 on Ni side, and Fig.10(b) shows the microstructure of representative points of A2, B2 and C2 on 304ss side. The locations of six representative points are illustrated in Fig.7(b). Besides, Solidification parameters of the six representative points are also calculated as shown in Fig.10. It can be obviously observed in 304ss side that the fine equiaxed dendrites, the coarse cellular dendrites and the planar appear at the top, the middle and the bottom area of the weld pool, respectively. On the Ni side, no planar crystal is observed but the trend of changes from equiaxed dendrites to fine cellular to coarse cellular dendrites are also observed at three representative points of A1, B1 and C1. As shown above, the experimentally observed results agree well with the tendency predicted from simulation.

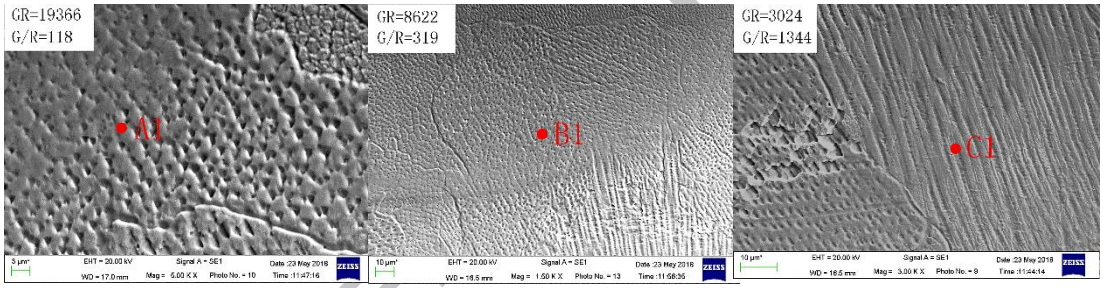

(a) Solidification microstructure in Ni side

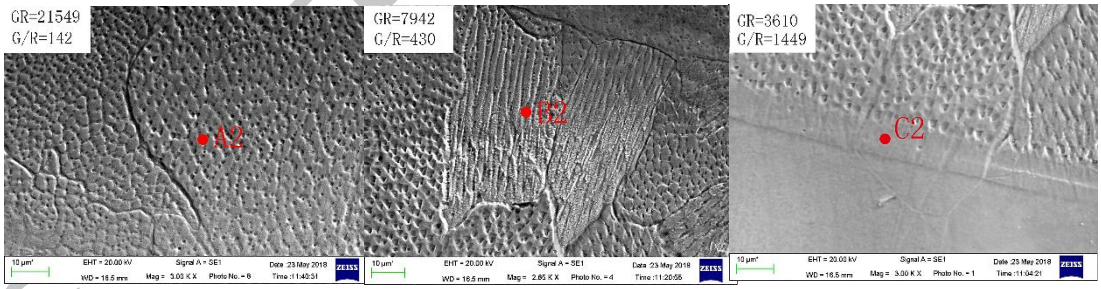

(b) Solidification microstructure in 304ss side

Fig.10 Microstructure for different locations in the weld pool. (a) Solidification microstructure in Ni side. (b) Solidification microstructure in 304ss side

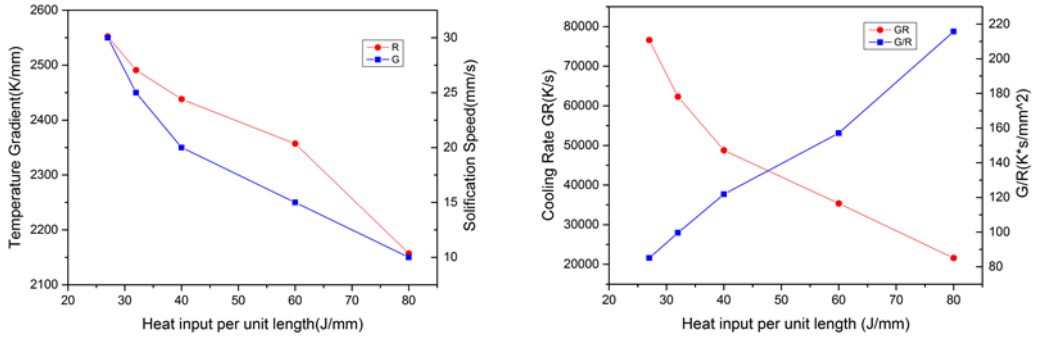

ACCEPTED MANUSCRIPT

(a) G and R (b) GR and G/R

Fig.11 Calculated solidification parameters at the weld centerline under different heat input per unit length. (a) G and R.（b) GR and G/R

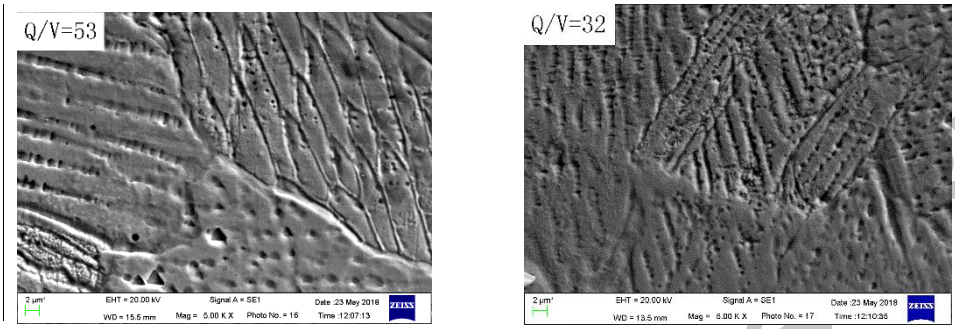

(a) 15mm/s (b) 25mm/s

Fig.12 Influence of welding speed on solidification microstructure in Ni side. (a)15mm/s.(b)25mm/s

The effects of welding speed on solidified microstructure are also studied in this work. Fig.11(a) shows the temperature gradient G and solidification rate R at the weld centerline for different heat input per unit length obtained by varying the weld speed from 10 to 30 mm/s and keeping the laser power a constant for 800W. The heat input per unit length of weld, E, is defined as the ratio of the heat input and the weld speed:

$$E = \frac{Q}{V} \tag{17}$$

where Q is the laser power, and V is the welding speed. With speed increasing from 10 to 30 mm/s, the ratio decreases from 80 to 26.7 J/mm , and both the temperature gradient and cooling rate increase.

As shown in Fig.11(b), the cooling rate(GR) decreases while the morphology parameter(G/R) increases at the weld centerline with the increase of E, which indicates that the finer equiaxed grains are more likely to be observed under higher speed in the fusion zone. As illustrated above, the solidification microstructure of the melt pool would be greatly affected by the welding speed and the change of cooling rate in this study is so significant that its effect on dimensions is unnegligible. Fig.12 summarizes the experimental observations of the solidification microstructure under different welding speed in Ni side. At the heat input of 800W, the solidification microstructure changes from coarse cellular to fine cellular when the welding speed increases from 15 to 25 mm/s.

ACCEPTED MANUSCRIPT

This phenomenon can also be explained by the heat conduction theory of welding and joining. According to equation $GR = -2\pi KV\frac{(T-T_0)^2}{Q}$ [26], which qualitatively tells the effect of welding parameters, cooling rates increase with decreasing Q/V and fine crystal structure results from higher cooling rate.

The simulations presented here include the thermal behavior in the melt pool, the free surface deformation and solidification characteristics predicted by the calculated solidification parameters with different welding parameters. The transient three-dimensional numerical model could be used to investigate the microstructure evolution of dissimilar metals under different welding parameters for various welding processes, such as laser welding, arc welding，electron beam welding and so on. In future study, the process parameters and mechanical properties，including hardness and tensile strength, can also be qualitatively linked through the computed solidification parameters to optimize process parameters and improve welding quality. Besides, the temperature field obtained by considering the flow of the molten pool can also be used as a temperature load on the finite element unit in the mechanical model to simulate the residual stress and deformation distribution of the dissimilar metal weldment.

Conclusion

A transient three-dimensional numerical model with heat transfer and fluid flow was developed for laser linear welding of 304ss and nickel. The heat transfer, the fluid flow, the free surface deformation and the melting-solidification with different welding speed were investigated both numerically and experimentally. The primary results of this study can be summarized as follows:

(1) At initial stage of the melt pool evolution, the Peclet number is small and the heat transfer is dominated by conduction, resulting in an approximately hemispherical melt pool on each side. As weld pool expands, Peclet number exceeds 46 due to the strong outward Marangoni convection, thus the dominant mechanism changes from conduction to convection, and the molten pool geometry evolves from circular to elliptical. The area of the melt pool in 304ss side is bigger than Ni side for the lower thermal conductivity and melting temperature. Resulting from stronger driving force, the maximum velocity in the molten pool generally appears at 304ss side when the weld pool reaches steady state.

(2) For the temperature evolution in the weld pool, the maximum temperature and cooling rate in 304ss side are significantly higher than those in nickel side due to the lower thermal conductivity. The temperature difference between the two points is smaller during the heating phase than the cooling phase, which is attributed to the Marangoni convection at heating stage.

(3) The free surface of the melt pool is captured by a moving mesh method based on the Arbitrary Lagrangian Eulerian (ALE). The simulated surface deformation is in good agreement with the

ACCEPTED MANUSCRIPT

experimental result. Sharp changes of the curvatures of the melt pool boundary are observed and explained by the Prandtl number. Since the calculated Pr is 0.25 for 304ss and 0.0028 for Ni, the fusion boundary in Ni side is approximately circular, while two inflexions of the fusion boundary in 304ss side could be obviously observed as the result of the competition of the heat conduction and the convection. Under the assumption of laminar flow, the calculated weld depth is generally over-predicted compared with experimental results, but the differences between the experimental results and the simulations are relatively small and acceptable.

(4) Since the G/R is bigger at the bottom and the GR is larger at the top surface，the microstructure morphology changes from equiaxed dendrites to cellular dendrites to planar , and grain size increases from the top to the bottom area of the weld pool in 304ss side. Similar tendency is also observed in Ni side. The heat input per unit length, Q/V, can also affect the solidification behavior and lower Q/V generally leads to finer scale of solidified microstructure.

Acknowledgements

The authors are grateful for the support from the National Natural Science Foundation of China under grant numbers 11272316, 11272317,11672304, and 11502269. In addition, the authors thank for the instrument developing project of the Chinese Academy of Sciences (No. yz201636).

Reference

1. M J Torkamany, S. Tahamtan, J Sabbaghzadeh (2010) Dissimilar welding of carbon steel to 5754 aluminum alloy by Nd:YAG pulsed laser. Mater Des 31(1): 458–465.

2. Yu G, He X L and Li S X (2017) Laser manufacturing and its application, National Defense Industry Press, Beijing.

3. J.P. Oliveira, Z. Zeng, C. Andrei, F.M. Braz Fernandes, R.M. Miranda, Antonio J. Ramirez, T. Omori, N. Zhou(2017) Dissimilar laser welding of superelastic NiTi and CuAlMn shape memory Alloys. Mater Design.128:166-175.

4. Qiang Jia, Wei Guo, Zhandong Wan, Yun Peng, Guisheng Zou, Zhiling Tian, Y. Norman Zhou (2018) Microstructure and mechanical properties of laser welded dissimilar joints between QP and boron alloyed martensitic steels. J Mater Process Tech 259:56-67.

5. Hui-Chi Chen, Andrew J. Pinkerton, Lin Li(2011) Fibre laser welding of dissimilar alloys of Ti-6Al-4V and Inconel 718 for aerospace applications. Int J Adv Manuf Technol 52:977–987.

6. Xiao Long Gao, Jing Liu, Lin Jie Zhang(2018) Dissimilar metal welding of Ti6Al4V and Inconel 718 through pulsed laser welding-induced eutectic reaction technology. Int J Adv Manuf Technol 96:1061–1071.

7. D Dong, Y Liu, L Wang, Y Yang, D Jiang, R Yang , W. Zhang(2016) Microstructure and deformation behavior of laser welded dissimilar dual phase steel joints. Sci Technol Weld Joi 21(2):75-82.

8. S Chakraborty, S Mukherjee, R Galun, Y Estrin, I Manna(2010) Transport phenomena in conduction mode laser beam welding of Fe-Al dissimilar couple with Ta diffusion barrier. Int J Heat Mass Transfer 53(23-24): 5274–5282.

9. W. Zhang, G. Roy, J. Elmer, T. DebRoy(2003) Modeling of heat transfer and fluid flow during gas tungsten arc spot welding of low carbon steel. J Appl Phys 93 (5):3022–3033.

10. A Farzadi, S Serajzadeh, A H Kokabi(2008) Modeling of heat transfer and fluid flow during gas tungsten arc welding of commercial pure aluminum. Int J Adv Manuf Technol

ACCEPTED MANUSCRIPT

38(3-4):258-267.
11. J W Liu, Z H Rao, S M Liao, H L Tsaib(2015) Numerical investigation of weld pool behaviors and ripple formation for a moving GTA welding under pulsed currents. Int J Heat Mass Transfer 91:990-1000.
12. W H Kim, S J Na(1998) Heat and fluid flow in pulsed current GTA weld pool. Int J Heat Mass Transfer 41(21):3213-3227.
13. Dae-Won Cho, Woo-Hyun Song , Min-Hyun Cho , Suck-Joo Na(2013) Analysis of submerged arc welding process by three-dimensional computational fluid dynamics simulations. J Mater Process Tech 213(12):2278-2291.
14. F Lu, X Tang, H Yu, S Yao(2006) Numerical simulation on interaction between TIG welding arc and weld pool. Comput Mater Sci 35 (4) :458–465.
15. A Traidia, F Roger(2011) Numerical and experimental study of arc and weld pool behavior for pulsed current GTA welding. Int J Heat Mass Transfer 54(9-10):2163-2179
16. Dae-Won Cho, Suck-Joo Na(2015) Molten pool behaviors for second pass V-groove GMAW. Int J Heat Mass Transfer 88:945-956.
17. J W Kim, S J Na(1994) A study on the three-dimensional analysis of heat and fluid flow in gas metal arc welding using boundary-fitted coordinates. Trans ASME J Eng Ind 116 :78–85.
18. A Bahrami, D Aidun, D Valentine(2014) Interaction of gravity forces in spot GTA weld pool. Welding J 93(4):139-144.
19. X He, P W Fuerschbach, T DebRoy(2003) Heat transfer and fluid flow during laser spot welding of 304 stainless stee. J Phys D: Appl Phys.36:1388–1398.
20. R Rai, J W Elmer, T A Palmer，T DebRoy（2007）Heat transfer and fluid flow during keyhole mode laser welding of tantalum Ti–6Al–4V, 304L stainless steel and vanadium. J Phys D: Appl Phys.40(18):5753-5766.
21. Alireza Bahrami, Daniel T Valentine, Brian T Helenbrook, Daryush K Aidun(2015) Study of mass transport in autogenous GTA welding of dissimilar metals. Int J Heat Mass Transfer 85: 41-53.
22. P S Wei, F K Chung(2000) Unsteady Marangoni flow in a molten pool when welding dissimilar metals. Metall Mater Trans B 31(6):1387–1403.
23. Yaowu Hu, Xiuli He, Gang Yu, Shusen Zhao(2016) Capillary convection in pulsed butt welding of miscible dissimilar couple. J Mech Sci Technol 231(13): 2429-2440.
24. LL Wang, JH Wei, ZM Wang(2018) Numerical and experimental investigations of variable polarity gas tungsten arc welding. Int J Adv Manuf Technol95(5-9): 2421-2428.
25. J C Lippold(2014) Welding Metallurgy and Weldability. John Wiley & Sons, New York.
26. S Kou(2003) Welding Metallurgy. John Wiley & Sons, New York.
27. R K C Chan (1975) A generalized arbitrary Lagrangian-Eulerian method for incompressible flows with sharp interfaces. J Comput Phys17(3): 311–331.
28. Mhamed Souli, David J Benson(2010)Abitrary Lagrangian Eulerian and Fluid-Structure Interaction. WILEY, United States.
29. Zhengtao Gan, Gang Yu, Xiuli He, Shaoxia Li(2017) Numerical simulation of thermal behavior and multicomponent mass transfer in indirect laser deposition of Co-base ally on steel. Int J Heat Mass Transfer104:28-38.
30. Nilanjan Chakraborty(2009) The effects of turbulence on molten pool transport during melting

ACCEPTED MANUSCRIPT

and solidification processes in continuous conduction mode laser welding of copper–nickel dissimilar couple. Appl Therm Eng29(17-18): 3618–3631.

31. A Nayar(1997) The Metals Databook, McGraw-Hill, New York.

32. P W Fuerschbach, G R Eisler(2002) Effect of laser spot weld energy and duration on melting and absorption, Sci Technol Weld Joining 7: 241–24.

33. V Voller, C Prakash(1987) A fixed grid numerical modelling methodology for convection–diffusion mushy region phase-change problems. Int J Heat Mass Transfer 30(8): 1709–1719.

34. Brent A D, Voller V R and Reid K J(1988) Eethalphy-Porosity technology for modeling convection-diffusion phase-change - application to the melting of a pure metal. Numer Heat Transfer 13(3): 297-318.

ACCEPTED MANUSCRIPT